## PAPER

Check for updates

# Recovery of tetrodotoxin from pufferfish viscera extract by amine-functionalized magnetic nanocomposites †

Dang Thuan Tran, ✳[a] Cam Van T. Do,[b] Cuc T. Dinh,[a] Mai T. Dang,[a] Khanh Hy Le Ho,[c] Truong Giang Le[ad] and Viet Ha Dao[cd]

Tetrodotoxin (TTX) has been widely used in pharmacology, food poisoning analysis, therapeutic use, and neurobiology. In the last decades, the isolation and purification of TTX from natural sources (*e.g.*, pufferfish) were mostly based on column chromatography. Recently, functional magnetic nanomaterials have been recognized as promising solid phases for the isolation and purification of bioactive compounds from aqueous matrices due to their effective adsorptive properties. Thus far, no studies have been reported on the utilization of magnetic nanomaterials for the purification of TTX from biological matrices. In this work, an effort has been made to synthesize $Fe_3O_4@SiO_2$ and $Fe_3O_4@SiO_2-NH_2$ nanocomposites for the adsorption and recovery of TTX derivatives from a crude pufferfish viscera extract. The experimental data showed that $Fe_3O_4@SiO_2-NH_2$ displayed a higher affinity toward TTX derivatives than $Fe_3O_4@SiO_2$, achieving maximal adsorption yields for 4epi-TTX, TTX, and Anh-TTX of 97.9, 99.6, and 93.8%, respectively, under the optimal conditions of contact time of 50 min, pH of 2, adsorbent dosage of 4 g $L^{-1}$, initial adsorbate concentration of 1.92 mg $L^{-1}$ 4epi-TTX, 3.36 mg $L^{-1}$ TTX and 1.44 mg $L^{-1}$ Anh-TTX and temperature of 40 °C. Interestingly, desorption of 4epi-TTX, TTX, and Anh-TTX from $Fe_3O_4@SiO_2-NH_2$-TTX investigated at 50 °C was recorded to achieve the highest recovery yields of 96.5, 98.2, and 92.7% using 1% AA/ACN for 30 min reaction, respectively. Remarkably, $Fe_3O_4@SiO_2-NH_2$ can be regenerated up to three cycles with adsorptive performance remaining at nearly 90%, demonstrating a promising adsorbent for purifying TTX derivatives from pufferfish viscera extract and a potential replacement for resins used in column chromatography-based techniques.

## 1 Introduction

Tetrodotoxin (TTX) is a nonprotein neurotoxin, one of the most toxic natural toxins ($LD_{50} = 8-11$ μg $kg^{-1}$) at lethal doses of 1–2 mg by the gastrointestinal tract for humans.[1–3] This compound has a strong affinity and specific sodium channel blocker effect,[4] leading to neurotransmission paralysis and TTX exhibits a very strong central analgesic effect.[2,5] More recently, TTX is being studied as an analgesic treatment for cancers. Clinical trials in several patients have shown that TTX has a significant analgesic effect.[6] One of the most recognizable species containing TTX toxin and its analogs is the pufferfish. It

has been broadly used in pharmacology,[7,8] food poisoning analysis,[9–11] therapeutic use (*e.g.*, anesthetic, epinephrine, bupivacaine, potential pain killer)[5,12] and neurobiology.[13]

Although TTX has displayed a wide application in relieving pain (*e.g.*, neuropathic pain, cancer-related pain),[14] neurophysiological disorders, and therapeutic usage,[12,15,16] it owns some limitations due to high cost of raw TTX-producing source, extraction, and purification. Methanol, ethanol, and acetic acid were common organic solvents used for extraction of TTX.[17,18] Moreover, solid materials, such as activated carbon, Bio-Rex 70 ($H^+$ form), Bio-Gel P2, and Resin have been conventionally used as solid phases for purification of TTX.[17,18] Despite numerous successful isolations, there have been no further advancements in the TTX purification process using column chromatography over the last decades.[19]

Nanomaterial is a class of material having one or more external dimensions in the range of 1–100 nm.[20] Due to their small size, nanostructures exhibit a high specific surface area with multiple properties such as optical, electronic, magnetic, catalytic, and adsorptive activities.[21] All these novel properties could potentially revolutionize many application fields.[22] Among those properties, the adsorptive characteristic of

*aInstitute of Chemistry, Vietnam Academy of Science and Technology (VAST), 18 Hoang Quoc Viet, Cau Giay, Hanoi 100000, Vietnam. E-mail: tdangthuan@ich.vast.vn*

*bHaUI Institute of Technology, Hanoi University of Industry (HaUI), 298 Cau Dien, Bac Tu Liem, Hanoi, Vietnam*

*cInstitute of Oceanography, Vietnam Academy of Science and Technology (VAST), 01 Cau Da St., Nha Trang City 650000, Vietnam*

*dGraduate University of Science and Technology (GUST), Vietnam Academy of Science and Technology (VAST), 18 Hoang Quoc Viet, Cau Giay, Hanoi 100000, Vietnam*

† Electronic supplementary information (ESI) available. See DOI: https://doi.org/10.1039/d3ra02166a

nanomaterials has been applied for adsorption of different compounds in environmental, biological, and food samples.[21] In order to enhance adsorption yield and capacity, nanomaterial is usually functionalized with different functional groups, such as amine, carboxylic, *etc.*, *via* covalent or noncovalent approach to enhance its affinity toward targeted molecules and compounds.[23,24] The functionalized surface of nanomaterial drives various applications.[21–23,25–27] Moreover, nanomaterials with magnetic properties have ease of regeneration and recycling, offering a great achievement in the enhancement of the adsorption of compounds from different matrices.[28] For instance, grafting of tris [2-(dimethylamino) ethyl] amine (Me$_6$TREN) onto the surface of SiO$_2$-coated Fe$_3$O$_4$ nanoparticles demonstrated a high adsorption efficacy with good selectivity of heavy metals from wastewater, while the magnetic core Fe$_3$O$_4$ allowed for the repeated recycling of the material.[29] Notably, Fe$_3$O$_4$@Me$_6$TREN NPs can be regenerated by desorbing heavy metal ions from NPs with EDTA sodium salt, which will be of great significance for cost reduction and further industrial applications.[29] Functional magnetic nanocomposites, including Fe$_3$O$_4$–NH$_2$@MIL-101, Fe$_3$O$_4$–COOH@MIL-101, and Fe$_3$O$_4$/C@MIL-101, synthesized by a hydrothermal method have been successfully applied for enrichment of estrogens (*e.g.*, estrone (E1), 17β-estradiol (E2), estriol (E3), and bisphenol-A (BPA)) in environmental water samples.[30] Magnetite@silica nanoparticles grafted with aminoterminated supramolecular cucurbit [6] uril pseudorotaxane complexes are shown to be highly efficient sorbent for salvianolic acids.[31] Particularly, extraction and isolation of bioactive compounds by adsorption phenomena using nanomaterials is one of the novel reported method due to its simplicity and high effectiveness.[32] A modification of Fe$_3$O$_4$@SiO$_2$ with (3-aminopropyl)trimethoxysilane (APTMS) and alginate (AA) forming nanocomposites Fe$_3$O$_4$@SiO$_2$–NH$_2$ and Fe$_3$O$_4$@SiO$_2$–NH$_2$-AA exhibited a higher adsorption capability of alkaloids (*e.g.*, palmatine and berberine) when compared to that of unmodified Fe$_3$O$_4$@SiO$_2$.[33] Magnetic nanoparticles grafted with (3-aminopropyl)triethoxysilane (APTES) were also used to load anticancer drug of Nintedanib for controlled release as a drug delivery system.[34] Moreover, functional magnetic nanomaterials are also used for extraction and mycotoxins, pesticides, and pharmaceuticals in food commodities[28] and adsorption/sensing of active ingredients in medicine.[32]

To date, there are no studies on the recovery of tetrodotoxin from pufferfish viscera extract using magnetic nanomaterials. Sequential adsorption and desorption of TTX derivatives on functionalized nanomagnetic material is a promising extraction and purification approach. The TTX derivatives have a greater tendency with positive ion groups (*e.g.*, –NH$_2$) by strong electrostatic interactions between amine groups of the TTX molecules. Hence, the fabrication of positive ion groups-functionalized nanoparticles enables the adsorption of TTX analogues effectively.

Therefore, the objectives of this study are to (i) to synthesize amine-functionalized nanocomposite material (Fe$_3$O$_4$@SiO$_2$–NH$_2$) and (ii) to optimize adsorption and desorption conditions of TTX derivatives from a pufferfish viscera extract. In this work,

magnetic core (Fe$_3$O$_4$) was synthesized by co-precipitation of ferric precursors followed by deposition of a silica shell on its surface by hydrolysis of tetraethyl orthosilicate (TEOS) to form nanocomposite Fe$_3$O$_4$@SiO$_2$.[33] The composite material Fe$_3$O$_4$@SiO$_2$ was then modified with amine-based high molecular weight molecule of (3-aminopropyl) triethoxylsilane (APTES) *via* covalent bonding to form amine-functionalized Fe$_3$O$_4$@SiO$_2$ (Fe$_3$O$_4$@SiO$_2$–NH$_2$).[35] Fe$_3$O$_4$@SiO$_2$ and Fe$_3$O$_4$@SiO$_2$–NH$_2$ were then examined as adsorbents for adsorption of TTX analogues in a TTX-rich extract of pufferfish viscera. The effects of operational parameters such as adsorption time, pH, adsorbent dosage, initial adsorbate concentration, and temperature on the adsorption yield of TTX derivatives were investigated. Moreover, the effects of solvents on TTX derivatives recovery yield from desorption of Fe$_3$O$_4$@SiO$_2$ and Fe$_3$O$_4$@SiO$_2$–NH$_2$ bound to TTX derivatives and regeneration of the adsorbents were also evaluated.

## 2. Experimental

### 2.1. Chemicals and reagents

Iron(II) chloride (FeCl$_2$·4H$_2$O) (99%), iron(III) chloride hexahydrate (FeCl$_3$·6H$_2$O) (99%), acetic acid (99.8%), hexane (99.5%), diethyl ether (99.5%), and ethanol (99.9%) were obtained from Samchun Chemical Co., Ltd. (Seoul, Republic of Korea). Ammonia solution (28%), tetraethyl orthosilicate (TEOS) (98%), (3-aminopropyl)triethoxysilane (APTES) (≥98%), and trichloroacetic acid (TCA) (99%) were obtained from Sigma Aldrich (Munich, Germany).

### 2.2. Pufferfish viscera sources and tetrodotoxin extraction

Pufferfish viscera sources were obtained from fishermen in the Can Gio coast, Ho Chi Minh City, Viet Nam, in December 2021. The pufferfish viscera were preserved and transferred to the Department of Technology of Bioactive Compounds, Institute of Chemistry, Vietnam Academy of Science and Technology. The viscera parts were frozen and stored below −20 °C until use. For toxin extraction, TTX derivatives were extracted according to modified procedures that were described by Brillantes *et al.*[36] and Dao *et al.*[37] Briefly, pufferfish viscera of 5 kg was thawed at room temperature, followed by mechanical grinding with 6 L of 1% acetic acid (v/v). The mixture was mechanically stirred overnight, followed by boiling under heat for 20 min for protein precipitation. The aqueous phase was separated from the mixture by pressing with a filter bag (with a pore size of 0.5 μm). The resulting extract was further processed for extraction of lipid and protein precipitation by hexane/diethyl ether (2/1, v/v) and trichloroacetic acid (30%), respectively. The final lipid- and protein-eliminated extract was preserved at 2–4 °C in a refrigerator for further experiments.

### 2.3. Preparation of Fe$_3$O$_4$, Fe$_3$O$_4$@SiO$_2$ and Fe$_4$O$_4$@SiO$_2$–NH$_2$

For Fe$_3$O$_4$, 1.52 g FeCl$_2$·4H$_2$O and 5.4 g FeCl$_3$·6H$_2$O were mechanically mixed in 200 mL deionized water at room temperature for 5 min. Then, the mixture was heated up to 85 °

C under mechanical stirring and purged with $N_2$ for 15 min, followed by the addition of 25 mL $NH_4OH$ and proceeding reaction for 1 h. The brown mixture turned to a black solution indicating $Fe^{2+}$ and $Fe^{3+}$ were converted to $Fe_3O_4$. The resultant material was harvested by a magnetic device and washed with deionized water and ethanol to neutral pH. The black precipitate was dried under reduced pressure at 40 °C for 5 h to obtain the dried sample for further experiments. For $Fe_3O_4@SiO_2$, 1 g $Fe_3O_4$ was dispersed in 160 mL absolute ethanol and 40 mL $H_2O$ in an ultrasound device for 30 min. The mixture was mechanically mixed at room temperature, followed by the addition of 10 mL $NH_4OH$ and stirring was maintained for 5 min. TEOS of 8 mL was dropwise added to the solution for hydrolysis and deposition reaction of $SiO_2$ on the surface of $Fe_3O_4$ for 12 h under room temperature conditions. The resulting $Fe_3O_4@SiO_2$ was magnetically harvested and repeatedly washed with deionized water and ethanol to neutral pH. The wet $Fe_3O_4@SiO_2$ was dried under reduced pressure at 40 °C for 5 h to obtain dry $Fe_3O_4@SiO_2$ for further experiments. For $Fe_3O_4@SiO_2–NH_2$ preparation, 2.5 g $Fe_3O_4@SiO_2$ was suspended in 150 mL toluene by ultrasound for 30 min, followed by dropwise addition of 10 mL APTES and the grafting reaction proceeded under a stirring rate of 150 rpm and temperature of 25 °C for 36 h. The resulting mixture was magnetically harvested and rinsed with ethanol ten times to completely remove unbound APTES. The synthesized $Fe_3O_4@SiO_2–NH_2$ material was dried under reduced pressure at 40 °C for 5 h to obtain the dried sample for further experiment.

### 2.4. Adsorption of TTX derivatives in pufferfish viscera extract by $Fe_3O_4@SiO_2$ and $Fe_3O_4@SiO_2–NH_2$

The adsorption of TTX from pufferfish viscera extract was performed by using the synthesized $Fe_3O_4@SiO_2$ and $Fe_3O_4@SiO_2–NH_2$ as adsorbents. Briefly, 10 mL of the pufferfish viscera extract (obtained from Section 2.2) containing 1.28 mg $L^{-1}$ 4epi-TTX, 2.24 mg $L^{-1}$ TTX, and 0.96 mg $L^{-1}$ Anh-TTX was loaded into a 100 mL cylindrical cup at 25 °C under stirring of 150 rpm, followed by the addition of $Fe_3O_4@SiO_2$ or $Fe_3O_4@SiO_2–NH_2$ at a concentration of 4 g $L^{-1}$ for adsorption of TTX. Various process parameters, including contact time, pH, dosage of $Fe_3O_4@SiO_2$ or $Fe_3O_4@SiO_2–NH_2$, initial concentration of TTX derivatives, and temperature, were investigated for maximal adsorption of TTX derivatives. The pH of the pufferfish viscera extract was adjusted from 2 to 10 with 2 M HCl or 2 M NaOH. Nanomaterial dosages used for investigation were in the range of 0–10 g $L^{-1}$. The equilibrium conditions for the adsorption of TTX derivatives onto $Fe_3O_4@SiO_2$ or $Fe_3O_4@SiO_2–NH_2$ were studied at different initial concentrations of TTX derivatives of 0.64 mg $L^{-1}$ 4epi-TTX, 1.12 mg $L^{-1}$ TTX, and 0.48 mg $L^{-1}$ Anh-TTX; 0.96 mg $L^{-1}$ 4epi-TTX, 1.68 mg $L^{-1}$ TTX, and 0.72 mg $L^{-1}$ Anh-TTX; 1.28 mg $L^{-1}$ 4epi-TTX, 2.24 mg $L^{-1}$ TTX, and 0.96 mg $L^{-1}$ Anh-TTX; 1.92 mg $L^{-1}$ 4epi-TTX, 3.36 mg $L^{-1}$ TTX, and 1.44 mg $L^{-1}$ Anh-TTX; and 2.81 mg $L^{-1}$ 4epi-TTX, 4.72 mg $L^{-1}$ TTX, and 1.93 mg $L^{-1}$ Anh-TTX for a contact time of 0–50 min. The temperature effect was investigated in the range of 25–80 °C. Samples were regularly taken at 5, 10, 15, 20,

30, 40, and 50 min for measurement of TTX derivative concentrations remaining in the suspension solution. $Fe_3O_4@SiO_2$ or $Fe_3O_4@SiO_2–NH_2$ absorbed with TTX derivatives were designated as $Fe_3O_4@SiO_2$-TTX and $Fe_3O_4@SiO_2–NH_2$-TTX, respectively. These materials were recovered from the experimental solution by an external electromagnet.

For desorption of TTX derivatives from $Fe_3O_4@SiO_2$-TTX and $Fe_3O_4@SiO_2–NH_2$-TTX, 50 mL of each solvent including 1% acetic acid/water (AA, 1% (v/v)), 1% acetic acid/methanol (AA/MeOH (1%, v/v)), 1% acetic acid/ethanol (AA/EtOH (1%, v/v)) or 1% acetic acid/acetonitrile (AA/ACN (1%, v/v)) was mixed with $Fe_3O_4@SiO_2$-TTX or $Fe_3O_4@SiO_2–NH_2$-TTX at a temperature of 50 °C and stirring rate of 150 rpm for 30 min to desorb TTX derivatives from the materials. TTX derivatives in the suspension solvent were analyzed for determination of TTX derivative recovery. The regenerated $Fe_3O_4@SiO_2$ and $Fe_3O_4@SiO_2–NH_2$ were repeatedly used for several adsorption and desorption cycles.

### 2.5. Determination of TTX derivative adsorption performance of $Fe_3O_4@SiO_2$ and $Fe_3O_4@SiO_2–NH_2$

The TTX derivative adsorption capacity ($q$), TTX derivative adsorption yield ($E$), and TTX derivative adsorption rate ($R$) of $Fe_3O_4@SiO_2$ and $Fe_3O_4@SiO_2–NH_2$ were calculated according to the following equations:

$$q = \frac{(C_0 - C_t)V}{m} \qquad (1)$$

$$E = \frac{(C_0 - C_t)}{C_0} \times 100 \qquad (2)$$

$$R = \frac{(C_0 - C_t)}{t} \qquad (3)$$

where $q$ is TTX derivative adsorption capacity (mg $g^{-1}$), $E$ is TTX derivative adsorption yield (%), $R$ is TTX derivative adsorption rate ($\mu$g $L^{-1}$ $min^{-1}$), $C_0$ is the initial concentration of TTX derivatives in pufferfish viscera extract (mg $L^{-1}$), $C_t$ is the concentration of TTX derivatives in pufferfish viscera extract measured at time slot $t$ (mg $L^{-1}$), $V$ is the volume of solution (L), and $m$ is the mass of adsorbent material (g).

### 2.6. Analysis

To determine TTX derivatives in pufferfish viscera extract, the extract obtained from Section 2.2 was priorly treated using an ENVI-carb SPE cartridge 250 mg (Sigma Aldrich Japan, Tokyo, Japan), diluted by four-fold diluted acetonitrile.[37] TTX derivatives were quantified by using a protocol and hydrophilic interaction liquid chromatography-mass spectrometer (HILIC/MS-MS) coupled with Shimadzu system triple-quadrupole mass spectrometer (LCMS-8040; Shimadzu Corporation, Kyoto, Japan) that were described by Dao *et al.*[38] The HILIC separation was performed using a Waters Xbrige (HILIC) Amide column (4.6 mm I.D × 150 mm, 3.5 μm) at 60 °C with 5 μl sample volume injected. Mobile phases were water/formic acid/ammonium hydroxide (500 : 0.075 : 0.3 v/v/v) (A); acetonitrile/water/formic acid (700 : 300 : 0.1 v/v/v) (B) with a flow rate of 0.6 mL $min^{-1}$.

The chromatographic conditions consisted of initial conditions 100% B, held for 20 min, followed by a linear gradient 50 : 50 A and B within 15 min, held for 9.90 min. Ion source parameters of MS spectrometer were as follows: Entrance Potential (EP): 10 V; Curtain gas (CUR): 30 psi; Ion Spray Voltage (IS): 4500 V; source desolvation temperature (TEM): 250 °C; source ion block temperature: 400 °C; desolvation gas flow: 1000 L h$^{-1}$, Nebulizer gas flow: 2 L min$^{-1}$; collision gas flow rate: 0.15 mL min$^{-1}$. Multiple reaction monitoring (MRM) was performed in positive electrospray ionization (ESI$^+$). A minimum of two transitions were used for each STX analogue. For each target ion, MRM ion channels were selected for specific product ions generated from the selected precursor ion.[36] To confirm TTX derivatives in the extract of pufferfish viscera, MS/MS spectra were obtained at −25 eV of collision energy with $m/z$ 320.1 > 302.1 for TTX and 4epi-TTX, $m/z$ 302.0 > 284.1 for Anh-TTX in the 1st transition; and −40 eV with $m/z$ 320.1 > 162.1 for TTX and 4epi-TTX, $m/z$ 302.0 > 162.0 for Anh-TTX in the 2nd transition. TTX derivative contents were calculated from HILIC-MS/MS data using standard curves and expressed in mg L$^{-1}$.[39] Validation of the accuracy of the HILIC-MS/MS methodology for quantification of TTX derivatives in pufferfish viscera extract was described in detail in the electronic ESI (ESI†).

Morphological characteristics of Fe$_3$O$_4$, Fe$_3$O$_4$@SiO$_2$, Fe$_3$O$_4$@SiO$_2$–NH$_2$, Fe$_3$O$_4$@SiO$_2$-TTX, and Fe$_3$O$_4$@SiO$_2$–NH$_2$-TTX were analyzed by scanning electron microscopy (FE-SEM S-4800, Hitachi, Tokyo, Japan). The composition and distribution of surface elements of the nanomaterial samples were measured by energy-dispersive X-ray spectroscopy (EDS, 7593-H, HORIBA, UK) coupled to SEM. Crystal structures of Fe$_3$O$_4$, Fe$_3$O$_4$@SiO$_2$, Fe$_3$O$_4$@SiO$_2$–NH$_2$, Fe$_3$O$_4$@SiO$_2$-TTX, and Fe$_3$O$_4$@SiO$_2$–NH$_2$-TTX were analyzed by X-ray diffraction (XRD, D8- Advance, Bruker, Germany) at theta from 10 to 80°. Thermal properties of Fe$_3$O$_4$, Fe$_3$O$_4$@SiO$_2$, Fe$_3$O$_4$@SiO$_2$–NH$_2$, Fe$_3$O$_4$@SiO$_2$-TTX, and Fe$_3$O$_4$@SiO$_2$–NH$_2$-TTX were assayed by thermo gravimetric analysis (TGA, Labsys TGA1600, SETARAM, France) from room temperature to 900 °C at a heating rate of 10 °C min$^{-1}$ under nitrogen gas flow condition. Functional groups on Fe$_3$O$_4$, Fe$_3$O$_4$@SiO$_2$, Fe$_3$O$_4$@SiO$_2$–NH$_2$, Fe$_3$O$_4$@SiO$_2$-TTX, and Fe$_3$O$_4$@SiO$_2$–NH$_2$-TTX were characterized with an FT-IR analysis (Spectrum Two FT-IR Spectrometer, PerkinElmer, UK) for the scan range of 4000–400 cm$^{-1}$ at a resolution of 4 cm$^{-1}$.

## 2.7. Statistical analysis

Experiments were conducted in triplicate, and data were reported as mean ± standard deviation (SD). Statistical analysis was done using one-way ANOVA followed by post hoc Tukey's test (Graph pad V7) and a $p$-value of <0.05 was declared as significant. The statistical analysis was conducted using the software package MiniTab18 (Minitab Pty Ltd., Sydney, Australia).

# 3 Results and discussions

## 3.1. Characterization of materials

**3.1.1 Crystal structure of materials.** X-ray diffraction analysis results of Fe$_3$O$_4$, Fe$_3$O$_4$@SiO$_2$, Fe$_3$O$_4$@SiO$_2$–NH$_2$, Fe$_3$O$_4$@SiO$_2$-TTX, and Fe$_3$O$_4$@SiO$_2$–NH$_2$-TTX samples are presented in Fig. 1A. The results show that diffraction peaks appear at the 2theta angles of 30.09°, 35.42°, 43.05°, 53.39°, 56.94°, and 62.51°, corresponding to the planes (200), (311), (400), (422), (511), and (440), respectively, which are characteristic of the center-cubic phase of Fe$_3$O$_4$ found in magnetic nanomaterials (JCPDS card, file no. 19-0629). This result is also consistent with data reported by Kumar $et\ al.$[40] and Cheng $et\ al.$[41] Because the experiments were performed in an inert gas environment, the formation of Fe$_2$O$_3$ was not observed in the XRD spectrum. This is an outstanding advantage of the co-precipitation method, which aims to obtain a single-phase Fe$_3$O$_4$ material. The X-ray diffraction spectra shown in Fig. 1A also reveal that Fe$_3$O$_4$@SiO$_2$, Fe$_3$O$_4$@SiO$_2$–NH$_2$, Fe$_3$O$_4$@SiO$_2$-TTX, and Fe$_3$O$_4$@SiO$_2$–NH$_2$-TTX materials still retain the same crystal structure as the Fe$_3$O$_4$ material. It is noteworthy that Fe$_3$O$_4$@SiO$_2$, Fe$_3$O$_4$@SiO$_2$–NH$_2$, Fe$_3$O$_4$@SiO$_2$-TTX, and Fe$_3$O$_4$@SiO$_2$–NH$_2$-TTX materials did not display the appearance of SiO$_2$ crystals in the XRD pattern. However, the chemical composition data of these materials measured by EDS detected Si with a mass content of 15.69–25.79% (Table 1 and Fig. 2B–E). This is logical because XRD only detects crystals of materials, whereas the SiO$_2$ layer coated over the Fe$_3$O$_4$ surface is an amorphous non-crystalline form. The materials Fe$_3$O$_4$@SiO$_2$–NH$_2$, Fe$_3$O$_4$@SiO$_2$-TTX, and Fe$_3$O$_4$@SiO$_2$–NH$_2$-TTX were surface modified and/or adsorbed with TTX derivatives, so organic elements, including N and C, are presented in their chemical compositions. Therefore, the EDS pattern of Fe$_3$O$_4$@SiO$_2$–NH$_2$, Fe$_3$O$_4$@SiO$_2$-TTX, and Fe$_3$O$_4$@SiO$_2$–NH$_2$-TTX measured both organic elements of C and N with mass proportions of 4.13–4.66 and 6.77–6.91%, respectively (Table 1 and Fig. 2C–E).

**3.1.2 Morphology of materials.** Fig. 2F–J shows the representative SEM images of Fe$_3$O$_4$, Fe$_3$O$_4$@SiO$_2$, Fe$_3$O$_4$@SiO$_2$–NH$_2$, Fe$_3$O$_4$@SiO$_2$-TTX, and Fe$_3$O$_4$@SiO$_2$–NH$_2$-TTX. It is observed that Fe$_3$O$_4$ particles are agglomerated and made ball-shaped particles and are relatively uniform (Fig. 2F).[42] The Fe$_3$O$_4$@SiO$_2$ particles contrast darkly due to the crystal field nature of Fe$_3$O$_4$ cores, which are distributed in SiO$_2$ with light contrast. The morphology of Fe$_3$O$_4$@SiO$_2$ is spherical shape and uniform.

The silica layer not only helps the magnetic core to be stable, avoiding corrosion, but also keeps the core Fe$_3$O$_4$ from leaching during the entire course of the reaction. Surface modification of −NH$_2$ functional groups and/or adsorption of TTX derivatives onto the surface of nanomaterials did not alter the shape and structure of the nanoparticles, as shown in Fig. 2H–J.

**3.1.3 Magnetic characteristics of the materials.** The curves of magnetization $versus$ magnetic field (M-H loop) of Fe$_3$O$_4$, Fe$_3$O$_4$@SiO$_2$, Fe$_3$O$_4$@SiO$_2$–NH$_2$, Fe$_3$O$_4$@SiO$_2$-TTX, and Fe$_3$O$_4$@SiO$_2$–NH$_2$-TTX are displayed in Fig. 1B. The data shows that the Fe$_3$O$_4$ material owns a magnetization of up to 54 emu g$^{-1}$ saturated in the external magnetic field region of −15000–15 000 Oe. This value is lower than the magnetization of bare Fe$_3$O$_4$ (68.78 emu g$^{-1}$) synthesized by Kumar $et\ al.$ (2022)[40] and super-paramagnetic cubic Fe$_3$O$_4$ materials (92 emu g$^{-1}$) reported by Liu $et\ al.$ (2019).[43] After coating of SiO$_2$ layer, Fe$_3$O$_4$@SiO$_2$ material achieved a reduced magnetization of 22
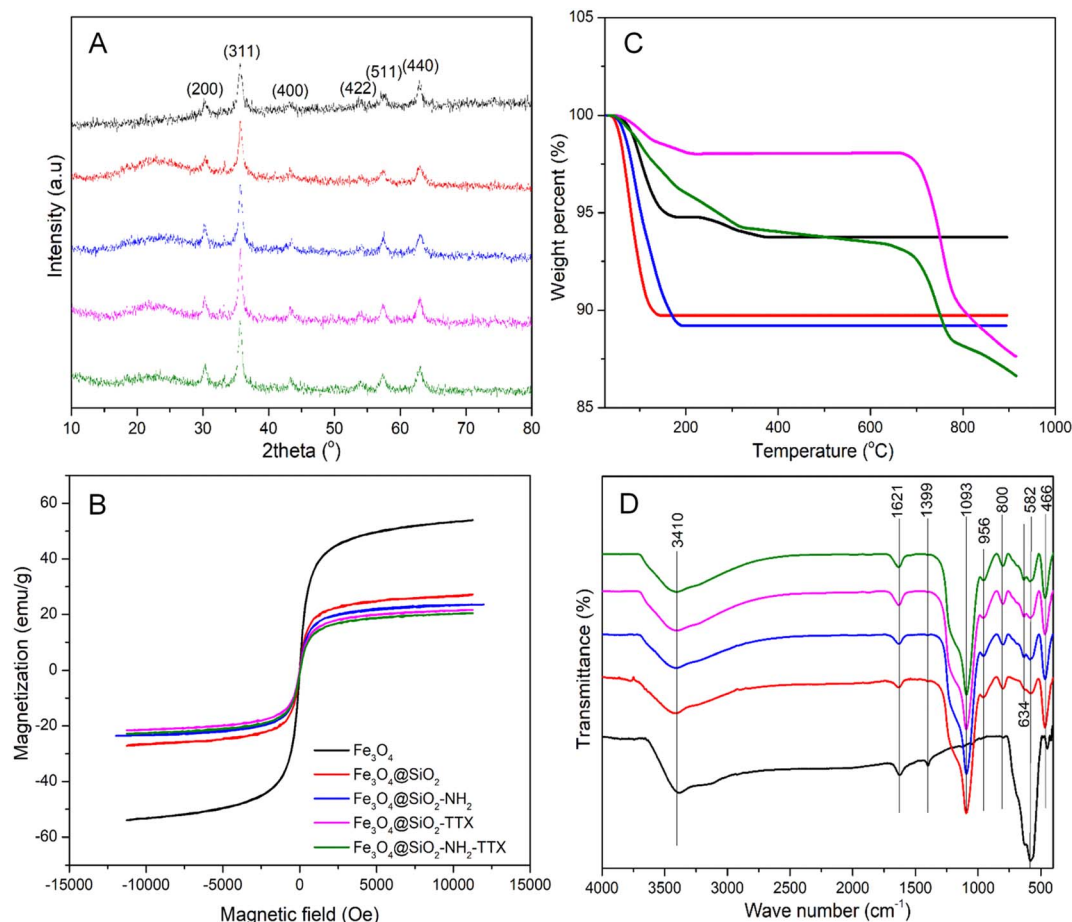
**Fig. 1** Characteristics of $Fe_3O_4$, $Fe_3O_4@SiO_2$, $Fe_3O_4@SiO_2-NH_2$, $Fe_3O_4@SiO_2$-TTX, $Fe_3O_4@SiO_2-NH_2$-TTX. XRD (A), VSM (B), TGA (C), and FT-IR (D).

**Table 1** Chemical composition analysis of materials by SEM-EDS[a]

| Element (%) | $Fe_3O_4$ | $Fe_3O_4@SiO_2$ | $Fe_3O_4@SiO_2-NH_2$ | $Fe_3O_4@SiO_2$-TTX | $Fe_3O_4@SiO_2-NH_2$-TTX |
|---|---|---|---|---|---|
| C | ND | ND | $4.13 \pm 0.38$ | $4.66 \pm 0.71$ | $4.22 \pm 0.64$ |
| N | ND | ND | $6.77 \pm 0.54$ | $6.88 \pm 1.03$ | $6.91 \pm 1.07$ |
| O | $39.46 \pm 2.45$ | $46.52 \pm 5.83$ | $43.26 \pm 1.01$ | $43.88 \pm 10.58$ | $44.00 \pm 5.49$ |
| Si | ND | $25.69 \pm 1.75$ | $16.92 \pm 0.33$ | $15.66 \pm 0.33$ | $15.81 \pm 0.63$ |
| Fe | $60.54 \pm 2.45$ | $27.79 \pm 4.72$ | $28.93 \pm 1.41$ | $28.91 \pm 10.43$ | $29.05 \pm 6.62$ |

[a] ND: not detected. TTX: tetrodotoxin.

emu $g^{-1}$. Moreover, grafting of $-NH_2$ groups and adsorption of TTX derivatives on $Fe_3O_4@SiO_2$ forming $Fe_3O_4@SiO_2-NH_2$, $Fe_3O_4@SiO_2$-TTX, and $Fe_3O_4@SiO_2-NH_2$-TTX materials with magnetization strength further decreased to 19–20 emu $g^{-1}$ (Fig. 1B). Despite the reduction of magnetization, the $Fe_3O_4@SiO_2$-TTX and $Fe_3O_4@SiO_2-NH_2$-TTX materials still own a high magnetic strength that is fairly sufficient for recovery and separation by favorable electromagnets for regeneration.

**3.1.4 Thermal properties of materials.** The thermal decomposition process of $Fe_3O_4$, $Fe_3O_4@SiO_2$, $Fe_3O_4@SiO_2-NH_2$, $Fe_3O_4@SiO_2$-TTX, and $Fe_3O_4@SiO_2-NH_2$-TTX recorded from room temperature to 900 °C is shown in Fig. 1C. The results show

that the $Fe_3O_4$ material lost 6% of its mass after increasing the heat to 400 °C and maintained a constant mass of 96% of its initial mass until 900 °C. The $Fe_3O_4@SiO_2$ was degraded up to 10% when the temperature increased to 150 °C and remained at about 90% initial mass until 900 °C. The proportion of decomposed matter of $Fe_3O_4@SiO_2-NH_2$ increased to more than 12% when the heat level increased to 200 °C and only maintained the mass below 89% when the temperature further increased to 900 °C. The $Fe_3O_4@SiO_2$-TTX and $Fe_3O_4@SiO_2-NH_2$-TTX materials resulted from the adsorption processes of $Fe_3O_4@SiO_2$ and $Fe_3O_4@SiO_2-NH_2$ and TTX derivatives, which are well-known as heat-stable compounds.[44] Thus, a strong decomposition of these

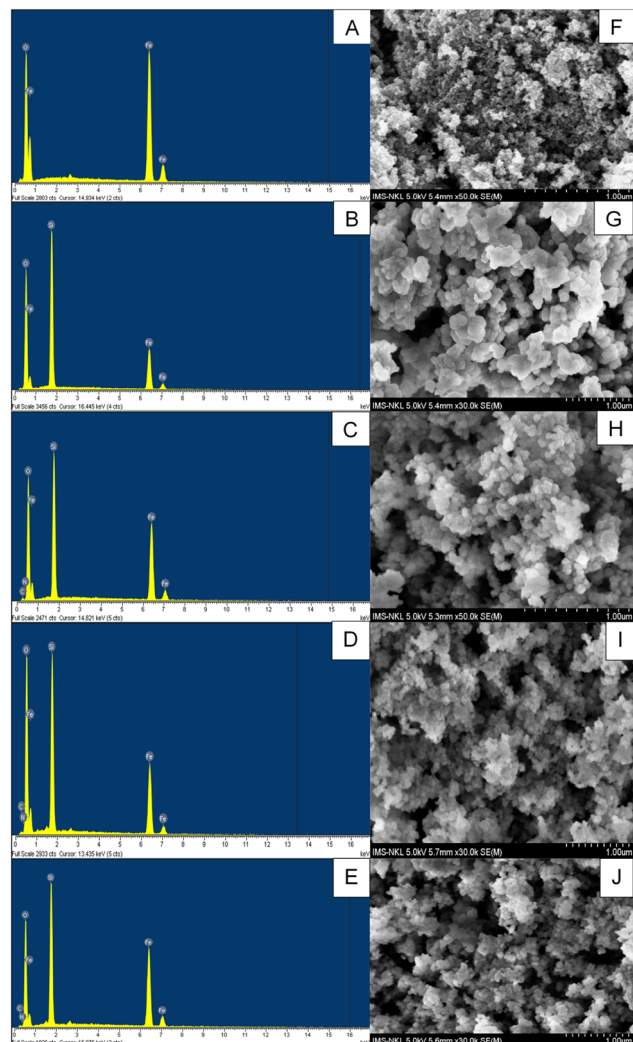**Fig. 2** EDS spectra of $Fe_3O_4$ (A), $Fe_3O_4@SiO_2$ (B), $Fe_3O_4@SiO_2-NH_2$ (C), $Fe_3O_4@SiO_2$-TTX (D), $Fe_3O_4@SiO_2-NH_2$-TTX (E) and SEM image of $Fe_3O_4$ (F), $Fe_3O_4@SiO_2$ (G), $Fe_3O_4@SiO_2-NH_2$ (H), $Fe_3O_4@SiO_2$-TTX (I), $Fe_3O_4@SiO_2-NH_2$-TTX (J).

materials was recorded from temperatures of up to 700 °C (Fig. 1C).

**3.1.5 Fourier transform infrared spectroscopy (FI-IR).** Fig. 1D shows the Fourier transform infrared spectra of samples $Fe_3O_4$, $Fe_3O_4@SiO_2$, $Fe_3O_4@SiO_2-NH_2$, $Fe_3O_4@SiO_2$-TTX, and $Fe_3O_4@SiO_2-NH_2$-TTX. Bare $Fe_3O_4$ nanoparticles show a strong peak at 582 cm$^{-1}$, belonging to the stretching vibration of the Fe–O bond, which is characteristic of $Fe_3O_4$ nanomaterials.[40] In addition, there are apparent weak peaks at 634 cm$^{-1}$ for $Fe_3O_4@SiO_2$, $Fe_3O_4@SiO_2-NH_2$, $Fe_3O_4@SiO_2$-TTX, and $Fe_3O_4@SiO_2-NH_2$-TTX, demonstrating that formation of a small amount of maghemite $Fe_2O_3$ ($\gamma$-$Fe_2O_3$) during $SiO_2$ deposition, $NH_2$ grafting, and TTX derivative adsorption processes, respectively.[42] The absorption bands at 3410 cm$^{-1}$ are associated with O–H stretching vibrations. Peaks appearing at 1621 cm$^{-1}$ are related to the deformed vibration of O–H.[35,45] These bands indicate the existence of hydroxyl groups connected to the surfaces of $Fe_3O_4$, $Fe_3O_4@SiO_2$, $Fe_3O_4@SiO_2-NH_2$,

$Fe_3O_4@SiO_2$-TTX, and $Fe_3O_4@SiO_2-NH_2$-TTX nanoparticles. The adsorption peaks appearing at 956 and 466 cm$^{-1}$ are assigned for the bending vibrations of Si–OH and Si–O–Si bonds, respectively.[40] The appearance of strong peaks at a wavelength of 1093 cm$^{-1}$ is characteristic of asymmetric and symmetric linear stretching vibrations of Si–O–Si bonds on $Fe_3O_4@SiO_2$, $Fe_3O_4@SiO_2-NH_2$, $Fe_3O_4@SiO_2$-TTX, and $Fe_3O_4@SiO_2-NH_2$-TTX.[40] The presence of Si–O–Si and Si–OH bonds is proof that $SiO_2$ is successfully coated onto $Fe_3O_4$ nanoparticles by chemical bonds. In addition, the adsorption band centered at 800 cm$^{-1}$ is the vibration of the C–C bond that is generated from organic compounds such as APTES grafted onto $Fe_3O_4@SiO_2$ ($Fe_3O_4@SiO_2-NH_2$) and TTX adsorbed onto $Fe_3O_4@SiO_2$ ($Fe_3O_4@SiO_2$-TTX) and $Fe_3O_4@SiO_2-NH_2$ nanoparticles ($Fe_3O_4@SiO_2-NH_2$-TTX). Apparently, the FT-IR analysis of $Fe_3O_4$, $Fe_3O_4@SiO_2$, $Fe_3O_4@SiO_2-NH_2$, $Fe_3O_4@SiO_2$-TTX, and $Fe_3O_4@SiO_2-NH_2$-TTX samples further confirmed that $Fe_3O_4$ synthesis, $SiO_2$ coating on $Fe_3O_4$, $NH_2$ grafting on $Fe_3O_4@SiO_2$, and TTX derivative adsorption on $Fe_3O_4@SiO_2$ and $Fe_3O_4@SiO_2-NH_2$ were successful.

### 3.2. TTX derivative contents in pufferfish viscera extract

Based on HPLC chromatograms of TTX standards (Fig. 3A) and TTX-rich pufferfish viscera extract (Fig. 3B), it is determined that the pufferfish viscera extract contains three basic derivatives of the TTX group, which are 4epi-TTX, TTX, and Anh-TTX. The content of 4epi-TTX, TTX, and Anh-TTX were determined as $2.81 \pm 0.07$, $4.72 \pm 0.05$, and $1.93 \pm 0.03$ mg L$^{-1}$ (Table 2), respectively. A high concentration of TTX derivatives indicates that pufferfish viscera extract is a promising source for TTX derivative purification using functional nanomaterials *via* adsorption–desorption protocol.

### 3.3. Adsorption characteristics of TTX derivatives on $Fe_3O_4@SiO_2$ and $Fe_3O_4@SiO_2-NH_2$

**3.3.1 Influence of contact time.** The adsorption of TTX derivatives by $Fe_3O_4@SiO_2$ and $Fe_3O_4@SiO_2-NH_2$ was investigated at different time intervals, and the results are presented in Fig. 4. It is shown that the concentrations of 4epi-TTX, TTX, and Anh-TTX decreased rapidly after exposure to $Fe_3O_4@SiO_2$ nanoparticles for the first 5–10 min. Thereafter, the concentrations of 4epi-TTX, TTX, and Anh-TTX decreased slowly to 0.60, 1.13, and 0.46 mg L$^{-1}$ for the prolonged time of 10–30 min, respectively. From 30 min onward, the concentrations of 4epi-TTX, TTX, and Anh-TTX tended to reach equilibrium levels of 0.58, 1.03, and 0.45 mg L$^{-1}$, respectively (Fig. 4A). $Fe_3O_4@SiO_2-NH_2$ nanoparticles demonstrated a greater affinity than $Fe_3O_4@SiO_2$ particles in adsorption of TTX compounds. The concentrations of 4epi-TTX, TTX, and Anh-TTX decreased from 1.28, 2.24, and 0.96 mg L$^{-1}$ to 0.47, 0.81, and 0.40 mg L$^{-1}$ for the first 20 min of reaction, followed by a gradual decrease to equilibrium levels of 0.42, 0.67, and 0.35 mg L$^{-1}$, respectively, when the reaction time reached 50 min (Fig. 4B). This data agrees well with adsorption trend of prodigiosin on amine-functionalized iron oxides, which also displayed reaching equilibrium at 50 min reaction using initial prodigiosin concentration of 1–10 g L$^{-1}$ at iron oxides
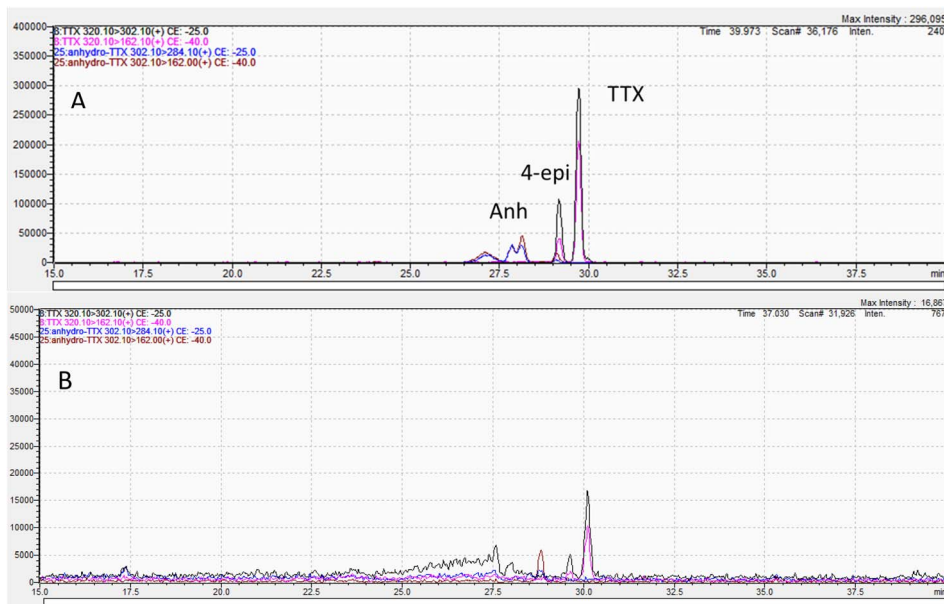
**Fig. 3** HPLC spectra of TTXs standards (A) and pufferfish viscera extract (B).

**Table 2** Content of TTX derivatives in the pufferfish viscera extract[a]

| Derivative | 4epi-TTX | TTX | Anh-TTX |
|---|---|---|---|
| Content (mg $L^{-1}$) | $2.81 \pm 0.07$ | $4.72 \pm 0.05$ | $1.93 \pm 0.03$ |

[a] Pufferfish viscera was collected from fishermen in the Can Gio coast, Ho Chi Minh City, Vietnam.

dosage of 20 g $L^{-1}$.[46] The adsorption yields of 4epi-TTX, TTX and Anh-TTX by $Fe_3O_4@SiO_2$ were determined as 53.3–54.9%, which were significantly lower than 63.3–70% measured for $Fe_3O_4@$-$SiO_2$–$NH_2$ ($p < 0.05$, Fig. 4C). The 4epi-TTX adsorption capacity of $Fe_3O_4@SiO_2$ and $Fe_3O_4@SiO_2$–$NH_2$ materials reached 0.18 and 0.22 mg $g^{-1}$, of which the maximum value of 0.22 mg $g^{-1}$ was determined for $Fe_3O_4@SiO_2$–$NH_2$ particles (Fig. 4D). Similarly, the TTX adsorption capacity of $Fe_3O_4@SiO_2$ and $Fe_3O_4@SiO_2$–$NH_2$ materials were 0.30 and 0.39 mg $g^{-1}$, respectively. Moreover, the Anh-TTX adsorption capacity of $Fe_3O_4@SiO_2$ and $Fe_3O_4@SiO_2$–$NH_2$ materials were 0.13 and 0.15 mg $g^{-1}$, respectively (Fig. 4D). The adsorption rate of TTX derivatives of $Fe_3O_4@SiO_2$–$NH_2$ reached 12.2–31.4 μg $L^{-1}$ $min^{-1}$, notably higher than 10.22–24.30 μg $L^{-1}$ $min^{-1}$ measured for $Fe_3O_4@SiO_2$ nanoparticles (Fig. 4E). Thus, it can be seen that $Fe_3O_4@SiO_2$ nanoparticles modified with amine (–$NH_2$) functional groups obviously shows higher affinity than $Fe_3O_4@SiO_2$ particles having only hydroxyl groups (–OH) on the surface. The achieved results are consistent with enhancement of adsorption efficiency and adsorption capacity of amine-grafted $Fe_3O_4$ for prodigiosin,[46] amino-terminated supramolecular cucurbit [6] uril pseudorotaxane complexes immobilized on magnetite@silica nanoparticles for salvianolic acids,[31] and amine-grafted $Fe_3O_4@SiO_2$ and amine-alginate-grafted $Fe_3O_4@SiO_2$ for alkaloids in comparison with ungrafted materials.[33] This is attributed to a principle that grafting more functional groups (e.g., amine,

carboxylic, etc.) on surfaces of the adsorbents creates intensively attractive forces from electrostatic interaction, van der Waals interaction, hydrophilic interaction, and hydrogen bonding between these groups and functional groups of targeted compounds.[32,47] Thus surface-modified nanomaterials usually display higher tendencies in the attachment of the targeted compounds when compared to that of unmodified counterparts.[48,49] It was noted that the equilibrium state of the adsorption of TTX derivatives by $Fe_3O_4@SiO_2$ and $Fe_3O_4@SiO_2$–$NH_2$ was about 50 min contacting time. Therefore, a reaction time of 50 min was chosen for further experiments.

**3.3.2 Influence of pH.** The pH value is an important factor that changes the surface charge of the absorbent materials in the solution, resulting in the adsorbents having different affinities for adsorbates under different pH conditions. The data shown in Fig. 5 illustrates that $Fe_3O_4@SiO_2$ and $Fe_3O_4@SiO_2$–$NH_2$ achieve maximum adsorption yield of TTX derivatives in acidic media with a pH level of 2. Increasing the pH value from 2 to 10 reduced the adsorption yield of TTX compounds.

Specifically, the adsorption yield of TTX compounds on $Fe_3O_4@SiO_2$ and $Fe_3O_4@SiO_2$–$NH_2$ at pH 2–3 reached 79–84 (Fig. 5A) and 89–99% (Fig. 5B), respectively. When solution pH increased to levels of 4–10, the adsorption yields of $Fe_3O_4@SiO_2$ and $Fe_3O_4@SiO_2$–$NH_2$ for TTX derivatives were significantly decreased to 34–71% ($p < 0.05$, Fig. 5A) and 45–85% ($p < 0.05$, Fig. 5B), respectively. This data is reasonable because TTX derivatives were successfully purified by most column chromatography packed with cation resins such as Bio-Rex 70 ($H^+$ form), Bio-Gel P2[17], and carboxylic acid form of HEMA.[50] This demonstrates that TTX derivatives exhibit a high affinity to cationic surface materials. From the data obtained, pH 2.0 was chosen for further experiments.

**3.3.3 Influence of adsorbent dosage.** When the dosage of adsorbent material increases, the adsorption yield increases
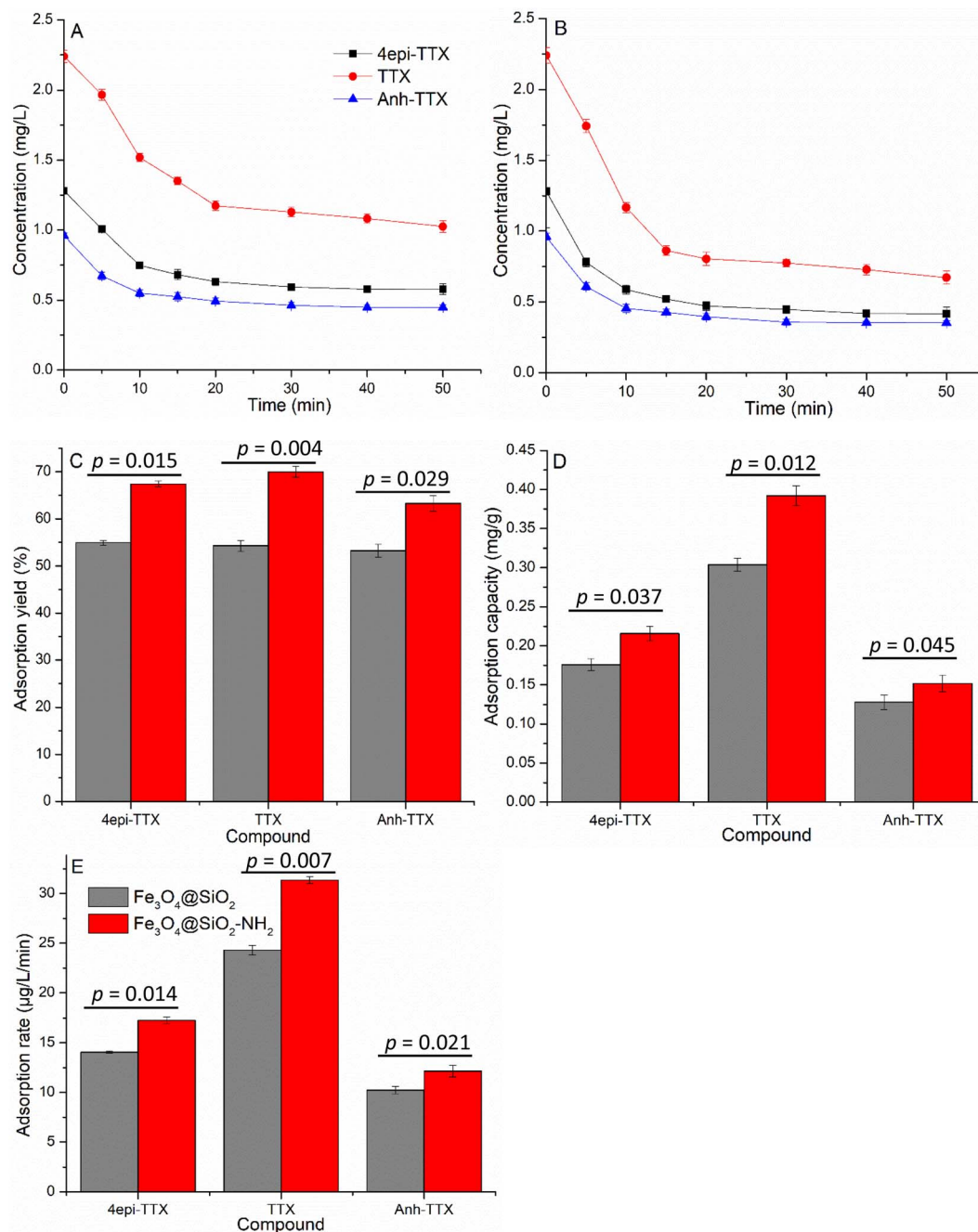
**Fig. 4** Variation of 4epi-TTX, TTX, and Anh-TTX concentrations over adsorption time by $Fe_3O_4@SiO_2$ (A) and $Fe_3O_4@SiO_2-NH_2$ (B), adsorption yield (C), adsorption capacity (D) and adsorption rate of $Fe_3O_4@SiO_2$ and $Fe_3O_4@SiO_2-NH_2$ (E). Adsorption conditions: temperature, 25 °C; pH, 7.0; stirring rate, 150 rpm; adsorbent dosage, 4 g $L^{-1}$; initial adsorbate concentrations, 1.28 mg $L^{-1}$ 4epi-TTX, 2.24 mg $L^{-1}$ TTX, and 0.96 mg $L^{-1}$ Anh-TTX.

due to an increase in the active surface area of the adsorbents in aqueous solution. However, for a defined concentration of adsorbate, the adsorption yield tends to reach a saturated level even if the adsorbent dosage increases further. On the other hand, the adsorption yield also depends on the natural characteristics of the adsorbent.

The data shown in Fig. 6 reveals that the adsorption yield for 4epi-TTX, TTX and Anh-TTX increases sharply from 0 to 80–83% as the dosage of $Fe_3O_4@SiO_2$ increases from 0 to 4 g $L^{-1}$

($p < 0.05$, Fig. 6A). Further increase in $Fe_3O_4@SiO_2$ dosage to higher than 4 g $L^{-1}$ resulted in a gradual enhancement of adsorption yield, which reached saturated levels of 90, 91, and 92% for 4epi-TTX, TTX, and Anh-TTX at the adsorbent dosage used, 10 g $L^{-1}$, respectively ($p > 0.05$, Fig. 6A). Similarly, a strong upward trend in adsorption yield was observed when $Fe_3O_4@SiO_2-NH_2$ dosage increased from 0 to 4 g $L^{-1}$ of, achieving 97, 97, and 98% for 4epi-TTX, TTX and Anh-TTX, respectively ($p < 0.05$, Fig. 6B). When $Fe_3O_4@SiO_2-NH_2$ dosage increased to
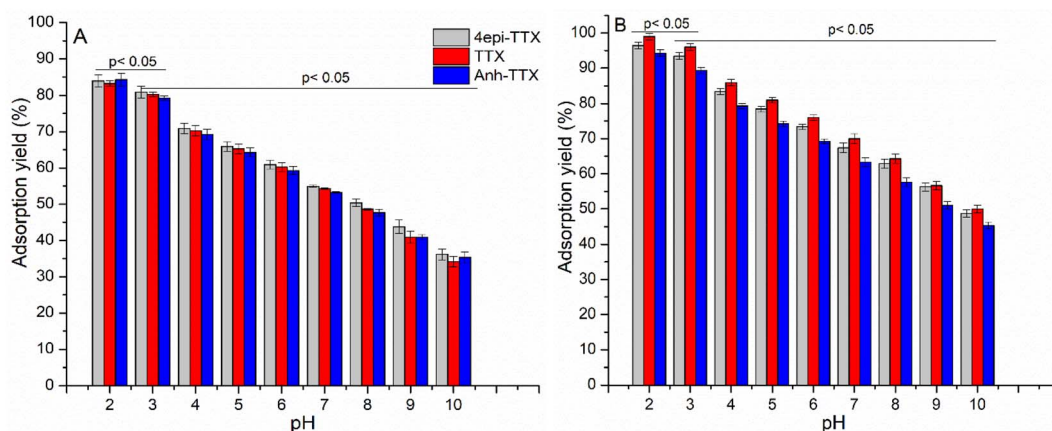
**Fig. 5** Adsorption yield of $Fe_3O_4@SiO_2$ (A) and $Fe_3O_4@SiO_2-NH_2$ (B) for 4epi-TTX, TTX, and Anh-TTX under different pH. Adsorption conditions: temperature, 25 °C; stirring rate, 150 rpm; adsorbent dosage, 4 g $L^{-1}$; initial adsorbate concentrations, 1.28 mg $L^{-1}$ 4epi-TTX, 2.24 mg $L^{-1}$ TTX and 0.96 mg $L^{-1}$ Anh-TTX; contact time, 50 min.
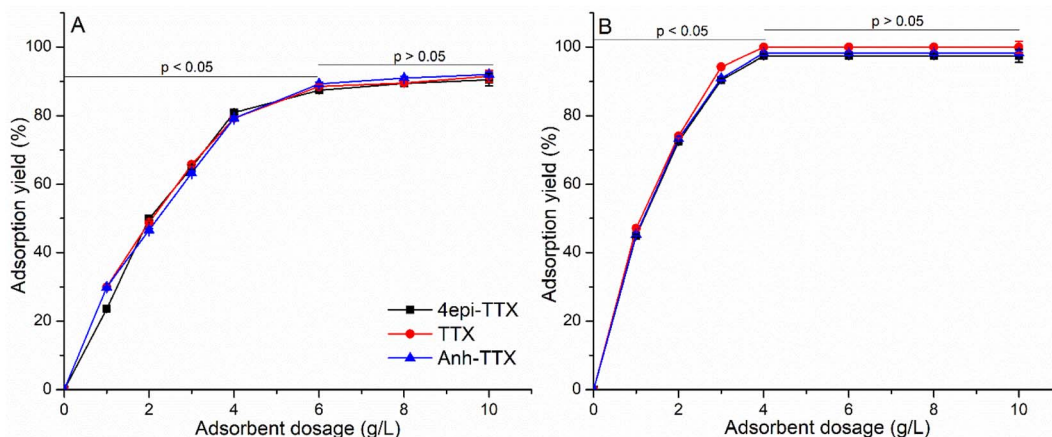


**Fig. 6** Adsorption yield of $Fe_3O_4@SiO_2$ (A) and $Fe_3O_4@SiO_2-NH_2$ (B) for 4epi-TTX, TTX and Anh-TTX under different $Fe_3O_4@SiO_2$ and $Fe_3O_4@SiO_2-NH_2$ dosages. Adsorption conditions: temperature, 25 °C; pH, 2.0; stirring rate, 150 rpm; initial adsorbate concentrations, 1.28 mg $L^{-1}$ 4epi-TTX, 2.24 mg $L^{-1}$ TTX and 0.96 mg $L^{-1}$ Anh-TTX; contact time, 50 min.

10 g $L^{-1}$, the adsorption yield for 4epi-TTX, TTX and Anh-TTX reached saturation levels of 97.4, 98, and 98.5%, respectively ($p > 0.05$, Fig. 6B). The adsorption data measured for $Fe_3O_4@SiO_2-NH_2$ demonstrated that grafting the $-NH_2$ functional group on $Fe_3O_4@SiO_2$ surface significantly improved the adsorption yield for TTX derivatives by 7% compared to that of $Fe_3O_4@SiO_2$ at the same adsorbent dosage used, which is 4 g $L^{-1}$ (Fig. 6B). The achieved results recommended the adsorbent dosage of 4 g $L^{-1}$ for further experiments.

**3.3.4 Effect of initial TTX derivatives concentration.** The increase in the concentration of adsorbates enhances the interaction possibility of adsorbates with active surfaces of adsorbent materials as the improvement of driving force for adsorbates to overcome the resistance of the mass transfer between the aqueous solution and the solid phase. At low concentrations, adsorption sites on adsorbents take up the available adsorbates quickly. Nevertheless, the adsorption capacity of adsorbent materials tends to reach a saturation limit

at high concentrations of adsorbates due to the increase of the resistance in aqueous solution and the reduction of available active sites on the surface of adsorbents.

Data shown in Fig. 7 reveals that when the concentration of 4epi-TTX increases from 0 to 1.28 mg $L^{-1}$, the adsorption capacity of $Fe_3O_4@SiO_2$ and $Fe_3O_4@SiO_2-NH_2$ increases linearly from 0 to levels of 0.296 and 0.312 mg $g^{-1}$, respectively. Increasing 4epi-TTX concentration to 1.92 mg $L^{-1}$ enhanced the 4epi-TTX adsorption capacity of $Fe_3O_4@SiO_2$ and $Fe_3O_4@SiO_2-NH_2$ by 0.374 and 0.451 mg $g^{-1}$, which gradually increased to 0.388 and 0.470 mg $g^{-1}$, respectively, as 4epi-TTX further increased to 2.81 mg $L^{-1}$ (Fig. 7A). For TTX and Anh-TTX, the studied concentrations were 0–4.72 and 0–1.93 mg $L^{-1}$, respectively. However, the linear trend of adsorption capacity of $Fe_3O_4@SiO_2$ and $Fe_3O_4@SiO_2-NH_2$ for TTX was observed at TTX concentration of 0–2.24 mg $L^{-1}$, followed by the second-order polynomial trend when initial TTX concentration further increased from 2.24 to 4.72 mg $L^{-1}$. The adsorption capacities
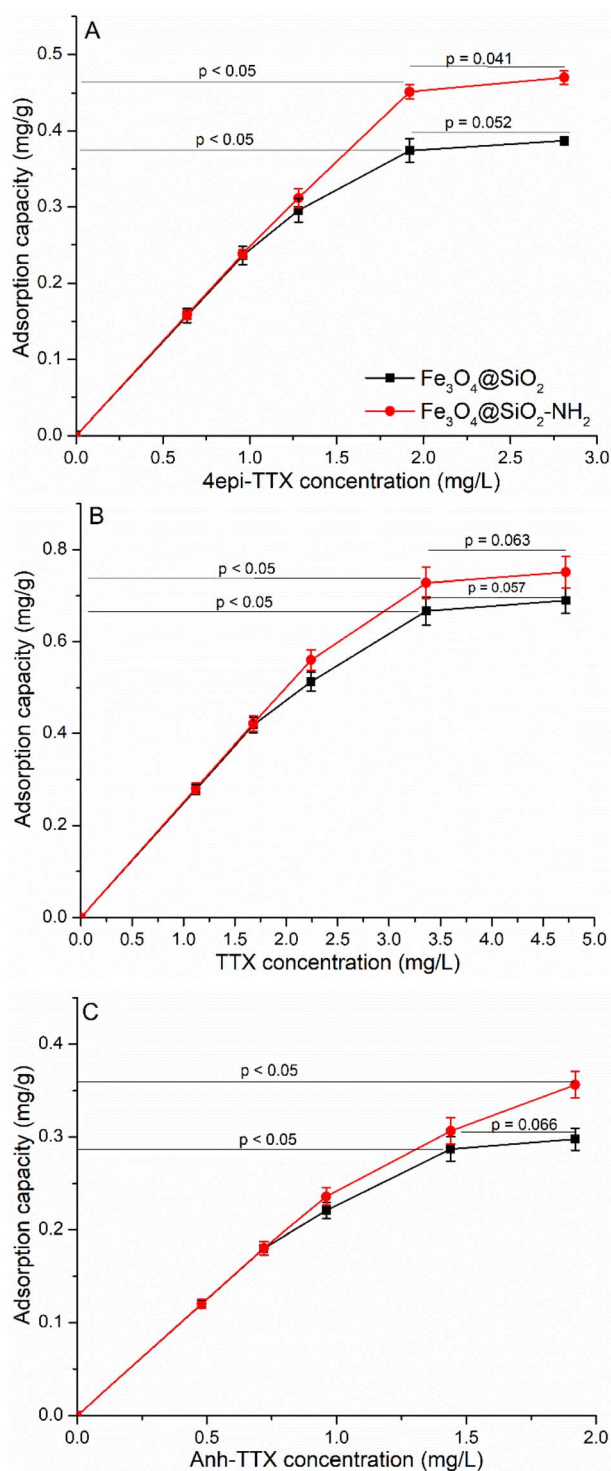
**Fig. 7** Adsorption capacity of $Fe_3O_4@SiO_2$ and $Fe_3O_4@SiO_2-NH_2$ for 4epi-TTX (A), TTX (B) and Anh-TTX (C) under different initial concentrations of 4epi-TTX, TTX, and Anh-TTX. Adsorption conditions: temperature, 25 °C; pH, 2.0; stirring rate, 150 rpm; adsorbent dosage, 4 g $L^{-1}$; contact time, 50 min.

of $Fe_3O_4@SiO_2$ and $Fe_3O_4@SiO_2-NH_2$ for TTX derivatives were measured as 0–0.670 and 0–0.751 mg $g^{-1}$ (Fig. 7B), respectively. The linear trend of adsorption capacity of $Fe_3O_4@SiO_2$ and

$Fe_3O_4@SiO_2-NH_2$ for Anh-TTX was observed at Anh-TTX concentration of 0–0.96 mg $L^{-1}$, followed by the second-order polynomial trend when initial Anh-TTX concentration further increased from 0.96 to 1.93 mg $L^{-1}$. The adsorption capacities of $Fe_3O_4@SiO_2$ and $Fe_3O_4@SiO_2-NH_2$ for Anh-TTX were 0–0.298 and 0–0.331 mg $g^{-1}$ (Fig. 7C), respectively. The obtained data recommend the initial adsorbate concentrations of 1.92 mg $L^{-1}$ 4epi-TTX, 3.36 mg $L^{-1}$ TTX, and 1.44 mg $L^{-1}$ Anh-TTX for further experiments.

**3.3.5 Influence of temperature.** Temperature is a critical factor affecting the adsorption capacity of adsorbents for molecules from aqueous solutions. Theoretically, adsorption decreases with an increase in temperature and molecules adsorbed earlier on a surface tend to desorb from the surface when temperature rises to elevated levels. However, the data shown in Fig. 8A shows that the adsorption yield of 4epi-TTX, TTX, and Anh-TTX on the $Fe_3O_4@SiO_2$ material increased from 87.9 to 93.6% when the temperature increased from 25 to 40 °C, then significantly decreased to 52.6–62.9% when the temperature further increased to 80 °C. This data demonstrated that a temperature of 40 °C was the best thermal condition to achieve a high adsorption yield of TTX derivatives on $Fe_3O_4@SiO_2$. This trend was also observed for $Fe_3O_4@SiO_2-NH_2$. In particular, the optimal adsorption temperature of $Fe_3O_4@SiO_2-NH_2$ for 4epi-TTX, TTX, and Anh-TTX was 40 °C, at which the TTX derivatives adsorption yields reached 93.8–99.6% (Fig. 8B). This data is in agreement with results reported for activated carbon, which exhibited maximal adsorption capacity of 52.63 and 59.02 mg $g^{-1}$ for $Pb^{2+}$ and $Cd^{2+}$, respectively, at a temperature of 40 °C. Temperatures lower or higher than 40 °C resulted in a decrease in adsorption capacity.[51] Similarity, activated carbon also exhibited an enhancement of adsorption for reactive dyes (e.g., C.I. Reactive Blue 2, C.I. Reactive Red 4, and C.I. Reactive Yellow 2) when temperature increased from 25 to 50 °C.[52] This is attributed to the principle that the increasing temperature simultaneously decreases the viscosity of the aqueous solution and increases molecular motion, allowing the uptake of molecules into the porous surface more easily, leading to increased adsorption as temperature increases. Nevertheless, further increase in temperature to over the optimal level causes desorption of molecules from the surface of materials. Hence, it was pointed out that the temperature of 40 °C was preferable for further adsorption experiments.

**3.4. Regeneration of $Fe_3O_4@SiO_2$ and $Fe_3O_4@SiO_2-NH_2$ and recovery of TTX derivatives**

Desorption of 4epi-TTX, TTX, and Anh-TTX from $Fe_3O_4@SiO_2$-TTX and $Fe_3O_4@SiO_2-NH_2$-TTX materials is necessary to recover TTX derivatives being utilized for various purposes as well as to regenerate $Fe_3O_4@SiO_2$ and $Fe_3O_4@SiO_2-NH_2$ for recycling. The desorption performance of 4epi-TTX, TTX, and Anh-TTX depends on the extraction solvents. As TTX derivatives are polar molecules, weakly polar desorption solvents, including acetonitrile (ACN), ethanol (EtOH), methanol (MeOH), and acetic acid (AA) were evaluated. The data shown in Fig. 9A illustrates that 1% AA/ACN solvent gives TTX derivative recovery yield of 91.7–93.6%,
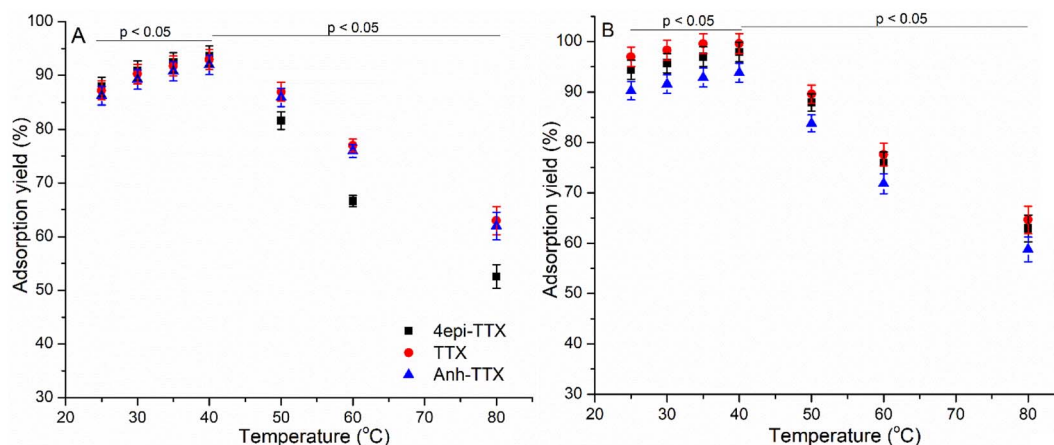
**Fig. 8** Adsorption yield of $Fe_3O_4@SiO_2$ (A) and $Fe_3O_4@SiO_2-NH_2$ (B) for 4epi-TTX, TTX, and Anh-TTX at different temperatures. Adsorption conditions: pH, 2.0; stirring rate, 150 rpm; adsorbent dosage, 4 g $L^{-1}$; initial adsorbate concentrations, 1.92 mg $L^{-1}$ 4epi-TTX, 3.36 mg $L^{-1}$ TTX, and 1.44 mg $L^{-1}$ Anh-TTX; contact time, 50 min.
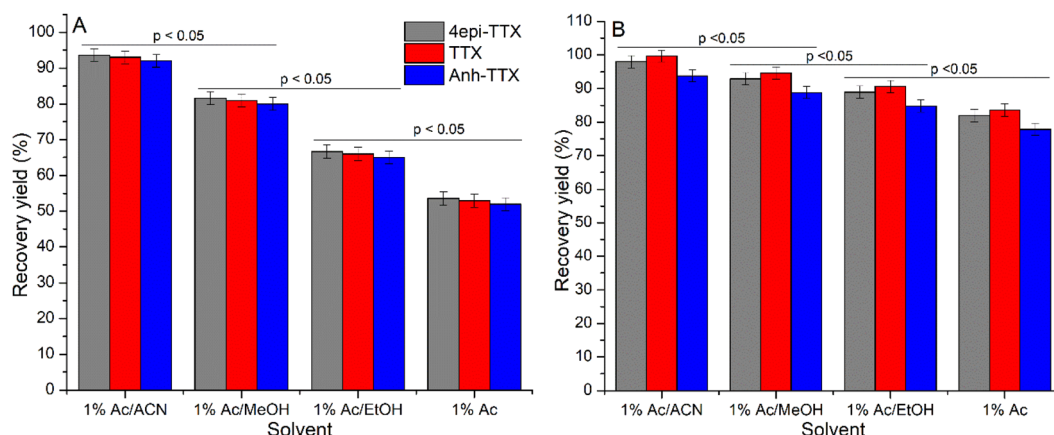


**Fig. 9** Recovery yield of 4epi-TTX, TTX, and Anh-TTX from $Fe_3O_4@SiO_2$-TTX (A) and $Fe_3O_4@SiO_2-NH_2$-TTX (B) using different solvents. Adsorption conditions: temperature, 40 °C; pH, 2.0; stirring rate, 150 rpm; adsorbent dosage, 4 g $L^{-1}$; initial adsorbate concentrations, 1.92 mg $L^{-1}$ 4epi-TTX, 3.36 mg $L^{-1}$ TTX, and 1.44 mg $L^{-1}$ Anh-TTX; contact time, 50 min. Desorption conditions: temperature: 50 °C, extraction time 30 min.

whereas 1% AA/MeOH, 1% AA/EtOH, and 1% AA only achieve 80–81.6, 65–66.6, and 52–53.6% from $Fe_3O_4@SiO_2$-TTX, respectively. The recovery yields of 4epi-TTX, TTX, and Anh-TTX from $Fe_3O_4@SiO_2-NH_2$-TTX by 1% AA/ACN, 1% AA/MeOH, 1% AA/EtOH, and 1% AA were determined as 92.7–98.2%, 88.8–94.6, 84.8–88.9, and 77.8–81.9%, respectively (Fig. 9B). Remarkably, TTX derivatives recovered from $Fe_3O_4@SiO_2$-TTX and $Fe_3O_4@SiO_2$-NH_2$-TTX using 1% AA/ACN solvent displayed high purity (Fig. 10A and B) when compared to that of the original crude extract (Fig. 3B), demonstrating that the synthesized nanocomposites, particularly $Fe_3O_4@SiO_2-NH_2$, were highly efficient adsorbents for recovery of TTX derivatives from pufferfish viscera extract without further chromatography-based purification.

The reuse of adsorbents is extremely important for economic optimization. The process of using adsorbent materials to isolate active ingredients many times causes deactivation of the superficial activity of the materials and leads to a decrease in the adsorption yield. The data presented in Fig. 11A shows that the

adsorption yields of $Fe_3O_4@SiO_2$ for 4epi-TTX, TTX, and Anh-TTX decrease sharply with the number of cycles, reducing from 80 to 10% when repeated cycles increase from 2nd to 7th, respectively. Notably, the $Fe_3O_4@SiO_2-NH_2$ material exhibited a dominant strength as it achieved an adsorption yield of nearly 90% after three cycles and considerably decreased to about 45% after 7 cycles (Fig. 11B).

Overall, optimal conditions for adsorption of TTX derivatives by $Fe_3O_4@SiO_2$ and $Fe_3O_4@SiO_2-NH_2$ from the pufferfish viscera extract were contact time of 50 min, pH 2, adsorbent dosage of 4 g $L^{-1}$, initial adsorbate concentration of 1.92 mg $L^{-1}$ 4epi-TTX, 3.36 mg $L^{-1}$ TTX and 1.44 mg $L^{-1}$ Anh-TTX, and temperature of 40 °C. For desorption of 4epi-TTX, TTX and Anh-TTX, the best solvent was 1% AA/ACN with the maximal recovery yield obtained under 50 °C for a 30 min reaction. The material $Fe_3O_4@SiO_2-NH_2$ was demonstrated to be a better adsorbent in the recovery of TTX derivatives from the crude pufferfish viscera extract when compared to $Fe_3O_4@SiO_2$.

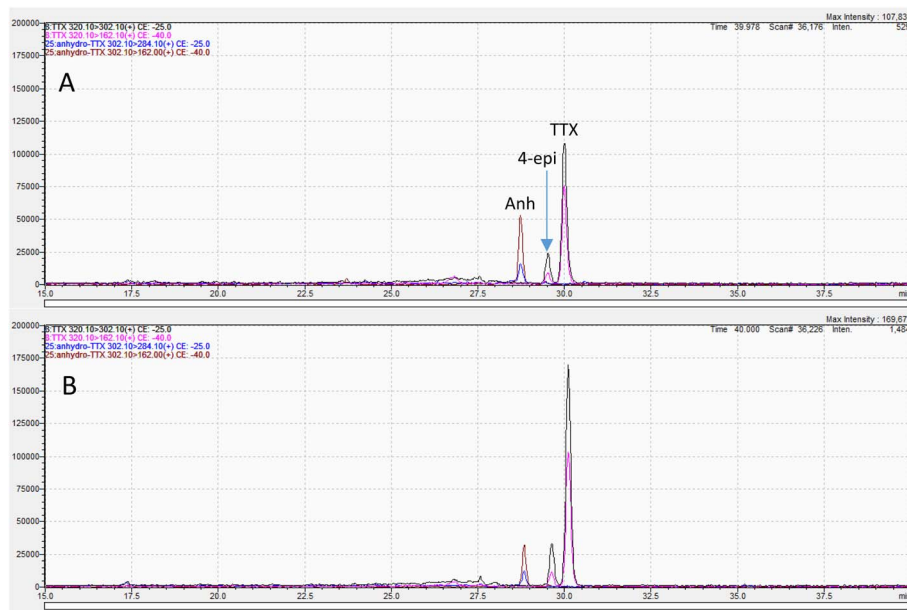**Fig. 10** HPLC spectra of 4epi-TTX, TTX, and Anh-TTX recovered from $Fe_3O_4@SiO_2$-TTX (A) and $Fe_3O_4@SiO_2-NH_2$-TTX (B) using 1% AA/ACN solvent.
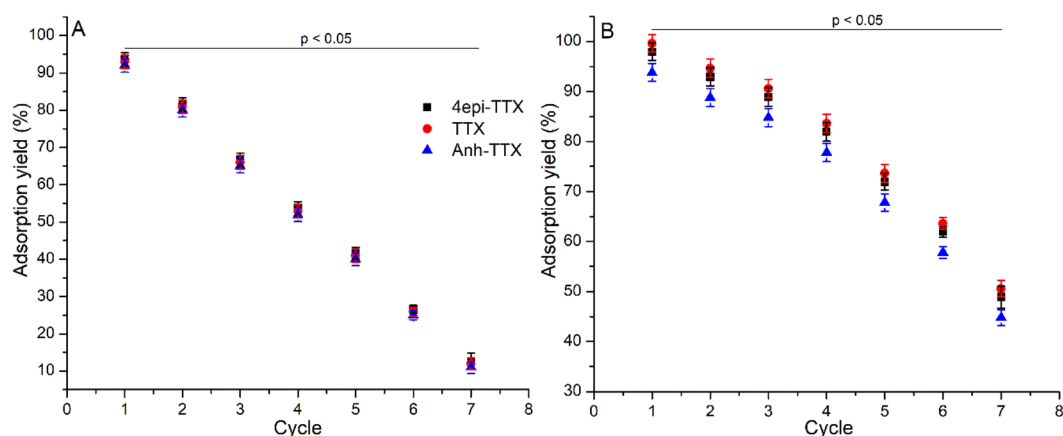


**Fig. 11** Adsorptive performance of $Fe_3O_4@SiO_2$ (A) and $Fe_3O_4@SiO_2-NH_2$ (B) for sequential adsorption and desorption of 4epi-TTX, TTX, and Anh-TTX. Adsorption conditions: temperature, 40 °C; pH, 2.0; stirring rate, 150 rpm; adsorbent dosage, 4 g $L^{-1}$; initial adsorbate concentrations, 1.92 mg $L^{-1}$ 4epi-TTX, 3.36 mg $L^{-1}$ TTX, and 1.44 mg $L^{-1}$ Anh-TTX; contact time, 50 min. Desorption conditions: solvent, 1% AA/CAN; temperature, 50 °C; extraction time 30 min.

## 4 Conclusions

We have successfully synthesized $Fe_3O_4@SiO_2$ and $Fe_3O_4@$-$SiO_2-NH_2$ and utilized them as adsorbents for the adsorption of TTX derivatives from crude pufferfish viscera extract. Among the materials, $Fe_3O_4@SiO_2-NH_2$ exhibited a higher affinity toward TTX derivatives during adsorption. The optimal conditions for adsorption of TTX derivatives onto $Fe_3O_4@SiO_2-NH_2$ were contact time of 50 min, pH 2, adsorbent dosage of 4 g $L^{-1}$, initial adsorbate concentrations of 1.92 mg $L^{-1}$ 4epi-TTX, 3.36 mg $L^{-1}$ TTX, and 1.44 mg $L^{-1}$ Anh-TTX, and temperature of 40 °C. Under the optimal conditions, $Fe_3O_4@SiO_2-NH_2$ achieved adsorption yields for 4epi-TTX, TTX, and Anh-TTX

were 93.8–99.6%. The highest recovery of 92.7–98.2% of 4epi-TTX, TTX, and Anh-TTX from $Fe_3O_4@SiO_2-NH_2$-TTX was recorded with 1% AA/ACN as the extracting solvent under 50 °C for a 30 min reaction. Remarkably, $Fe_3O_4@SiO_2-NH_2$ can be regenerated and reused to up to three cycles without significant loss of its original activity. The synthesized $Fe_3O_4@SiO_2-NH_2$ was demonstrated as a promising adsorbent for the isolation and purification of TTX derivatives from the pufferfish viscera extract without the use of column chromatography. Our future works are aimed at the synthesis of large amounts of $Fe_3O_4@SiO_2-NH_2$ for up-scale purification of TTX derivatives from the pufferfish viscera extract.

## Author contributions

## Conflicts of interest

There are no conflicts to declare.

## Acknowledgements

## References

1 Y. K. T Goto, S. Takahashi and Y. Hirata, *Tetrahedron*, 1965, **21**, 2059–2088.

2 S. I. K Tsuda, M. Kawamura, R. Tachikawa and K. Sakai, *Chem. Pharm. Bull.*, 1964, **12**, 1357–1374.

3 T. Noguchi and O. Arakawa, *Mar. Drugs*, 2008, **6**, 220–242.

4 C. H. Lee and P. C. Ruben, *Channels*, 2008, **2**, 407–412.

5 F. R. Nieto, E. J. Cobos, M. A. Tejada, C. Sanchez-Fernandez, R. Gonzalez-Cano and C. M. Cendan, *Mar. Drugs*, 2012, **10**, 281–305.

6 N. A. Hagen, B. Lapointe, M. Ong-Lam, B. Dubuc, D. Walde, B. Gagnon, R. Love, R. Goel, P. Hawley, A. H. Ngoc and P. Du Souich, *Curr. Oncol.*, 2011, **18**, e109–e116.

7 A. Leffler, R. I. Herzog, S. D. Dib-Hajj, S. G. Waxman and T. R. Cummins, *Pflugers Arch.*, 2005, **451**, 454–463.

8 T. Narahashi, *J. Toxicol. Toxin Rev.*, 2001, **20**, 67–84.

9 T. Noguchi, K. Onuki and O. Arakawa, *ISRN Toxicol.*, 2011, **2011**, 276939.

10 K. Tsujimura, H. Yoshimura, T. Taguri and H. Motomura, *Shokuhin Eiseigaku Zasshi*, 2017, **58**, 253–259.

11 T. Noguchi and O. Arakawa, *Mar. Drugs*, 2008, **6**, 220–242.

12 J. Lago, L. P. Rodríguez, L. Blanco, J. M. Vieites and A. G. Cabado, *Mar. Drugs*, 2015, **13**, 6384–6406.

13 M. H. Evans, *Int. Rev. Neurobiol.*, 1972, **15**, 83–166.

14 S. Islam, Z. Wang, Z. Zhou and W. Liu, *E3S Web of Conferences*, 2021, vol. 292, p. 03065.

15 P. Katikou, C. Gokbulut, A. R. Kosker, M. Campàs and F. Ozogul, *Mar. Drugs*, 2022, **20**, 47.

16 G. M. Bucciarelli, M. Lechner, A. Fontes, L. B. Kats, H. L. Eisthen and H. B. Shaffer, *Toxins*, 2021, **13**, 517.

17 A. Manabu, S. Yasuo, M. Keisuke and N. Tamao, in *Chromatography*, ed. C. Leonardo de Azevedo, IntechOpen, Rijeka, 2012, ch. 10, DOI: 10.5772/48668.

18 X. W. Chen, H. X. Liu, Y. B. Jin, S. F. Li, X. Bi, S. Chung, S. S. Zhang and Y. Y. Jiang, *Toxicon*, 2011, **57**, 938–943.

19 W. E. Houssen and M. Jaspars, in *Natural Products Isolation*, eds. S. D. Sarker and L. Nahar, Humana Press, Totowa, NJ, 2012, pp. 367–392, DOI: 10.1007/978-1-61779-624-1_14.

20 M. Fabbiani, F. Cesano, F. Pellegrino and C. Negri, *Molecules*, 2021, **26**, 7097.

21 R. Kecili and C. M. Hussain, in *Nanomaterials in Chromatography*, ed. C. M. Hussain, Elsevier, 2018, pp. 89–115, DOI: 10.1016/B978-0-12-812792-6.00004-2.

22 I. Khan, K. Saeed and I. Khan, *Arabian J. Chem.*, 2019, **12**, 908–931.

23 R. Bushra, in *Nanomaterials in Chromatography*, ed. C. M. Hussain, Elsevier, 2018, pp. 403–414, DOI: 10.1016/B978-0-12-812792-6.00015-7.

24 J. Comer, R. Chen, H. Poblete, A. Vergara-Jaque and J. E. Riviere, *ACS Nano*, 2015, **9**, 11761–11774.

25 M. B. Bhavya, S. Swain, P. Bhol, S. Yadav, A. Altaee, M. Saxena, P. K. Misra and A. K. Samal, in *Functionalized Nanomaterials for Catalytic Application*, 2021, pp. 109–134, DOI: 10.1002/9781119809036.ch4.

26 S. Palit and C. M. Hussain, in *Handbook of Functionalized Nanomaterials for Industrial Applications*, ed. C. Mustansar Hussain, Elsevier, 2020, pp. 3–14, DOI: 10.1016/B978-0-12-816787-8.00001-6.

27 S. Kanchi and K. Bisetty, in *Nanomaterials in Chromatography*, ed. C. M. Hussain, Elsevier, 2018, pp. 37–54, DOI: 10.1016/B978-0-12-812792-6.00002-9.

28 S. Targuma, P. B. Njobeh and P. G. Ndungu, *Molecules*, 2021, **26**, 4284.

29 J. Jing and C. Shi, *Molecules*, 2020, **25**, 3204.

30 Y.-F. Huang, M. Liu, Y.-Q. Wang, Y. Li, J.-M. Zhang and S.-H. Huo, *RSC Advances*, 2016, **6**, 15362–15369.

31 Q. Zhang, D. D. Zhou, J. W. Zhang, D. Gao, F. Q. Yang, H. Chen and Z. N. Xia, *Talanta*, 2019, **195**, 354–365.

32 J. Qian and G. Kai, *J. Pharm. Biomed. Anal.*, 2020, **190**, 113548.

33 L. Yang, J. Tian, J. Meng, R. Zhao, C. Li, J. Ma and T. Jin, *Molecules*, 2018, **23**, 562.

34 V. C. Karade, A. Sharma, R. P. Dhavale, R. P. Dhavale, S. R. Shingte, P. S. Patil, J. H. Kim, D. R. T. Zahn, A. D. Chougale, G. Salvan and P. B. Patil, *Sci. Rep.*, 2021, **11**, 5674.

35 Y. Li, H. Chen, J. Wu, Q. He, Y. Li, W. Yang and Y. Zhou, *Appl. Surf. Sci.*, 2018, **447**, 393–400.

36 S. Brillantes, W. Samosorn, S. Faknoi and Y. Oshima, *Fish. Sci.*, 2003, **69**, 1224–1230.

37 H. Dao Viet, L. H. K. Hy, T. S. H. Trinh, N. N. Tung and P. X. Ky, *Russ. J. Mar. Biol.*, 2023, **49**, 62–67.

38 V. H. Dao, H. K. H. Le and X. K. Pham, *AMA*, 2021, **51**, 1501–1507.

39 M. Nakamura and T. Yasumoto, *Toxicon*, 1985, **23**, 271–276.

40 A. P. Kumar, D. Bilehal, T. Desalegn, S. Kumar, F. Ahmed, H. C. A. Murthy, D. Kumar, G. Gupta, D. K. Chellappan, S. K. Singh, K. Dua and Y.-I. Lee, *Adsorp. Sci. Technol.*, 2022, **2022**, 3970287.

41 Y. Cheng, R. Tan, W. Wang, Y. Guo, P. Cui and W. Song, *J. Mater. Sci.*, 2010, **45**, 5347–5352.

42 A. Bali Ogholbeyg, A. Kianvash, A. Hajalilou, E. Abouzari-Lotf and A. Zarebkohan, *J. Mater. Sci.: Mater. Electron.*, 2018, **29**, 12135–12143.

43 X. Liu, S. Jiang, M. Niu, S. Li, W. Li and S. Yu, *J. Nanosci. Nanotechnol.*, 2019, **19**, 833–838.

44 K. Tsuda and M. Kawamura, *Pharm. Bull.*, 1953, **1**, 112–113.

45 T. K. H. Ta, M.-T. Trinh, N. V. Long, T. T. M. Nguyen, T. L. T. Nguyen, T. L. Thuoc, B. T. Phan, D. Mott, S. Maenosono, H. Tran-Van and V. H. Le, *Colloids Surf. A Physicochem. Eng. Asp.*, 2016, **504**, 376–383.

46 K. V. Arivizhivendhan, M. Mahesh, R. Boopathy, K. Patchaimurugan, P. Maharaja, S. Swarnalatha, R. Regina Mary and G. Sekaran, *J. Phys. Chem. B*, 2016, **120**, 9685–9696.

47 S. S. Nadar, P. D. Patil and N. M. Rohra, *Trends Food Sci. Technol.*, 2020, **103**, 225–238.

48 J. M. Goddard and J. H. Hotchkiss, *Prog. Polym. Sci.*, 2007, **32**, 698–725.

49 K. S. Yoha, S. R. Priyadarshini, J. A. Moses and C. Anandharamakrishnan, in *Green Nanomaterials: Processing, Properties, and Applications*, ed. S. Ahmed and W. Ali, Springer Singapore, Singapore, 2020, pp. 261–282, DOI: **10.1007/978-981-15-3560-4_11**.

50 Y. Shimizu, in *Natural Products Isolation*, ed. R. J. P. Cannell, Humana Press, Totowa, NJ, 1998, pp. 329–341, DOI: **10.1007/978-1-59259-256-2_11**.

51 M. H. Jnr and A. I. Spiff, *Electron. J. Biotechnol.*, 2005, **8**, 162–169.

52 Y. S. Al-Degs, M. I. El-Barghouthi, A. H. El-Sheikh and G. M. Walker, *Dyes Pigm.*, 2008, **77**, 16–23.